Title
Nanoscale Compositional and Strain Gradients Enable High-Speed and Amplitude-Resolved Pyroelectric Sensing

Journal
Advanced Materials, 38(44)

ISSN
0935-9648

Authors
Lin, Ching-Che
Park, Tae Joon
Bhat, Ashwath
et al.

Publication Date
2026-07-02

DOI
10.1002/adma.73909

Advanced Materials

ADVANCED MATERIALS
www.advmat.de

RESEARCH ARTICLE

Nanoscale Compositional and Strain Gradients Enable High-Speed and Amplitude-Resolved Pyroelectric Sensing

Ching-Che Lin[1,2] | Tae Joon Park[3,4] | Ashwath Bhat[5] | Tae Yeon Kim[1,2] | Djamila Lou[3] | Deokyoung Kang[2,3] | Zishen Tian[2,3] | Jiyeob Kim[1,2] | Sreekeerthi Pamula[2,3] | Jaegyu Kim[2,3] | Brendan Hanrahan[6] | Chris Dames[5] | Lane W. Martin[1,2,7]

[1]Department of Materials Science and NanoEngineereing, Rice University, Houston, Texas, USA | [2]Rice Advanced Materials Institute, Rice University, Houston, Texas, USA | [3]Department of Materials Science and Engineering, University of California, Berkeley, California, USA | [4]Department of Materials Science and Engineering, Korea University, Seoul, Republic of Korea | [5]Department of Mechanical Engineering, University of California, Berkeley, California, USA | [6]DEVCOM U.S. Army Research Laboratory, Adelphi, Maryland, USA | [7]Departments of Chemistry and Physics and Astronomy, Rice University, Houston, Texas, USA

Correspondence: Lane W. Martin (lwmartin@rice.edu)

Received: 24 March 2026 | **Revised:** 3 June 2026 | **Accepted:** 16 June 2026

Keywords: built-in potential | compositional gradient | high-frequency | pyroelectricity | relaxor ferroelectrics | thermal sensing | thin film | zero-bias operation

ABSTRACT

The frequency response of pyroelectric sensors is fundamentally governed by thermal time constant (τ_{th}, determined by thermal mass and thermal conductance) and electrical impedance arising from film capacitance and readout circuit. Conventional bulk $LiTaO_3$ detectors are optimized for high responsivity at low modulation frequencies (0.1–10 Hz), possessing a large τ_{th} that thermally averages rapid temperature oscillations at elevated modulation frequencies, limiting fidelity in resolving dynamic varying thermal signals. Here, compositional and strain gradients are introduced into 100-nm-thick relaxor-ferroelectric films reducing τ_{th} to ≈2 μs and producing built-in potentials (≈1.45 V or 145 kV cm^{-1}) that enhance the pyroelectric coefficient and suppress the dielectric constant. This enables complementary dual-mode operation by enhancing current-mode electrical responsivity and improving the voltage-mode figure of merit – advantageous for superior temperature resolution ($\Delta T_{\mathrm{min}} \approx 30$ μK). The responsivity peak shifts to near 1 kHz (>2500-times higher than conventional bulk sensors), with measurable responsivity extending to a carrier frequency of 100 kHz and amplitude-resolved detection at modulation frequencies up to 15 kHz. These results establish nanoscale internal-field engineering can reshape electro-thermal trade-off in pyroelectric thin films toward zero-bias, high-thermal-sensitivity, and amplitude-resolved thermal sensing across a wide frequency bandwidth.

1 | Introduction

Conventional pyroelectric-based thermal detectors are generally optimized for high responsivity at low modulation frequencies (sub-Hz to 10 Hz) for motion sensing [1], physiological monitoring [2], and gas analyzers [3]. These detectors are typically based on tens-to-hundreds of micrometers thick $LiTaO_3$ [4–9], $LiNbO_3$ [10, 11], and relaxor-ferroelectric crystals [12, 13], depending on device architecture and fabrication approach. In general, pyroelectric detection is governed by three factors: (1) *thermal sensitivity* (i.e., the average temperature oscillation amplitude experienced by the active layer, $\Delta T(\omega)$, averaged over film thickness, where ω is the modulation frequency), (2) *electrical responsivity*, which depends on the type of readout amplifier

Ching-Che Lin and Tae Joon Park contributed equally to this work.

employed – either current-mode or voltage-mode amplifiers can be used, but since both produce a voltage output, device performance in both modes is ultimately measured in volts of output per watt of incident radiation power (i.e., the current ($R_I = I_\pi / P_{in}$) or voltage ($R_V = V_\pi / P_{in}$) responsivity, where I_π is the pyroelectric current, V_π is the pyrovoltage after readout amplification, and P_{in} is the incident power), and (3) the *signal-to-noise ratio*, which depends on both the intrinsic pyroelectric material properties and the choice of voltage amplifier. In bulk pyroelectric materials, the frequency-dependent thermal response is governed by thermal diffusion and the device thermal boundary conditions. As the modulation frequency increases, the thermal-penetration depth decreases relative to the crystal thickness, progressively attenuating the thermal sensitivity, $\Delta T(\omega)$; a phenomenon which here will be referred to as *thermal blindness*. While specific device architectures modify the thermal boundary conditions (e.g., thermally isolated suspended membranes, substrate-mounted configurations, or vacuum/xenon-encapsulated structures), thickness-dependent penetration depth effects represent an intrinsic materials-level limitation governing high-frequency pyroelectric response.

Bulk pyroelectric detectors are typically designed to maximize the peak responsivity at low carrier frequencies by employing high-gain voltage amplification and thermal shielding to enhance thermal responsivity; such that even as the response rolls off at higher carrier frequencies, the time-averaged signal amplitude remains within a detectable range. This strategy does not, however, address another fundamental limitation: whether the detector can resolve the amplitude-fidelity of dynamic thermal profiles at high modulation frequencies – a distinction that becomes critical when the detector for the application must faithfully track transient or rapidly evolving thermal events rather than merely detecting their time-averaged presence. For thin-film devices directly deposited on a substrate, the thermal response is governed by both the thermal capacitance of the active layer and the thermal conductance to the substrate. Reducing the film thickness decreases the thermal capacitance and shortens the thermal equilibration time, thereby lowering the effective τ_{th} and shifting the peak responsivity toward higher modulation frequencies; however, this thickness scaling introduces an electrical trade-off since device capacitance ($C_D \propto 1/t_{film}$) suppresses voltage-mode responsivity, whereas current-mode responsivity becomes limited by amplifier noise [1]. These complementary characteristics reveal an inherent electrical-thermal trade-off and highlight the need for materials design strategies that not only rely on geometric thinning but also engineer intrinsic material properties including the pyroelectric coefficient ($\pi = dP/dT$, where P is the polarization) and dielectric constant (ε_r).

To overcome these challenges, nanoscale thin-film pyroelectric devices require simultaneous high thermal bandwidth together with high electrical responsivity – properties that are governed not only by intrinsic material parameters (e.g., π, ε_r, and volumetric heat capacity c_p) but also by device geometry and thermal design – demanding large π and high voltage figure of merit ($FoM_V = \pi / c_p \varepsilon_o \varepsilon_r$), where ε_o is the vacuum permittivity. Aluminum nitride (AlN) [14, 15] enables rapid thermal responses due to high thermal conductivity (≈285 W m^{-1} K^{-1}), but its low $\pi \approx -6$ to -8 μC m^{-2} K^{-1} [16] restricts pyroelectric conversion. Relaxor ferroelectrics (e.g., $0.68PbMg_{1/3}Nb_{2/3}O_3$-$0.32PbTiO_3$, PMN-0.32PT) exhibit much higher $\pi \approx -550$ μC m^{-2} K^{-1} under applied electric fields [17], values that exceed conventional ferroelectrics [e.g., $LiNbO_3$ ($\pi \approx -80$ μC m^{-2} K^{-1}) [18, 19], $LiTaO_3$ ($\pi \approx -173$ μC m^{-2} K^{-1}) [8, 12], and $PbZr_{0.2}Ti_{0.8}O_3$ ($\pi \approx -200$ μC m^{-2} K^{-1}) [20]. But PMN-0.32PT thin films typically suffer from two fundamental challenges: (1) low remanent polarization (P_r) necessitates external biasing and increases energy consumption for device operation, and (2) high ε_r (especially at zero bias), which suppresses FoM_V. Developing routes to "internally bias" (i.e., turn on a built-in electric field (E_{int}) which inherently biases the material) such relaxor ferroelectric thin films would be essential for zero-bias operation, simultaneously enhancing P_r and π while reducing ε_r.

In nanoscale ferroelectric thin films, E_{int} has been demonstrated as an effective means to control polarization and its response to external stimuli [21] (e.g., dielectricity, piezoelectricity, or pyroelectricity). Strategies include asymmetric electrodes with different work functions, defect-dipole-induced imprint (i.e., shifted polarization-electric field hysteresis loops) [22], multilayer heterostructures [23], or interface engineering such as Schottky junctions at the electrode/film interface [13, 24]. Strain-gradient engineering via compositional gradients has proven particularly effective at producing E_{int}. Compositionally graded $Ba_{1-x}Sr_xTiO_3$ films with $E_{int} \approx 25$ kV cm^{-1} exhibit thermally stable high $\varepsilon_r \approx 775$ with low loss across a 300°C window [25]. Large strain gradients ($\approx 4 \times 10^5$ m^{-1}) in compositionally graded $Pb_{1-x}Zr_xTiO_3$ films enhance piezoelectric response by introducing highly mobile ferroelastic domains [26]. For pyroelectrics, compositionally graded $Pb_{1-x}Zr_xTiO_3$ thin films exhibit improved FoM_V over uniform-composition counterparts (e.g., $PbZr_{0.2}Ti_{0.8}O_3$ thin films), primarily due to reduced ε_r from E_{int} [27]. Earlier studies on relaxor-ferroelectric films suggested that compositional nonuniformity can produce spatial distributions in Curie temperature and spontaneous polarization, thereby generating polarization gradients that lead to asymmetric charge transport and pseudopyroelectric behavior [28]. More recently, relaxor ferroelectrics have also been deliberately engineered via cation or oxygen-vacancy profiles across film thickness to enhance E_{int} and piezoelectric response [29, 30].

Here, a systematic approach combining modeling, nanoscale materials design, and direct electrothermal measurements realizes high-frequency pyroelectric sensing. Thickness-dependent thermal-electrical modeling elucidates how nanoscale scaling modifies the balance between thermal sensitivity and electrical responsivity. Guided by these insights, compositional gradients and epitaxial strain are engineered in nanoscale relaxor-ferroelectric-based pyroelectric films to induce E_{int} that achieve three key functionalities: (1) enhanced π, (2) suppressed ε_r, and (3) reduced electrical-time constant (τ_{el}) – which combine to produce simultaneous high electrical responsivity, extended thermal bandwidth, and zero-bias operation. Direct electrothermal measurements [17, 31] then quantify the pyroelectric response in both current- and voltage-mode readout configurations, revealing their complementary characteristics in voltage output amplitude and temperature detection resolution. This approach provides a nanoscale design approach that produces a 28-times improvement in FoM_V such that, at a 10 kHz carrier freqeucny, current-mode sensing yields a voltage output that is ≈ 20-times larger than

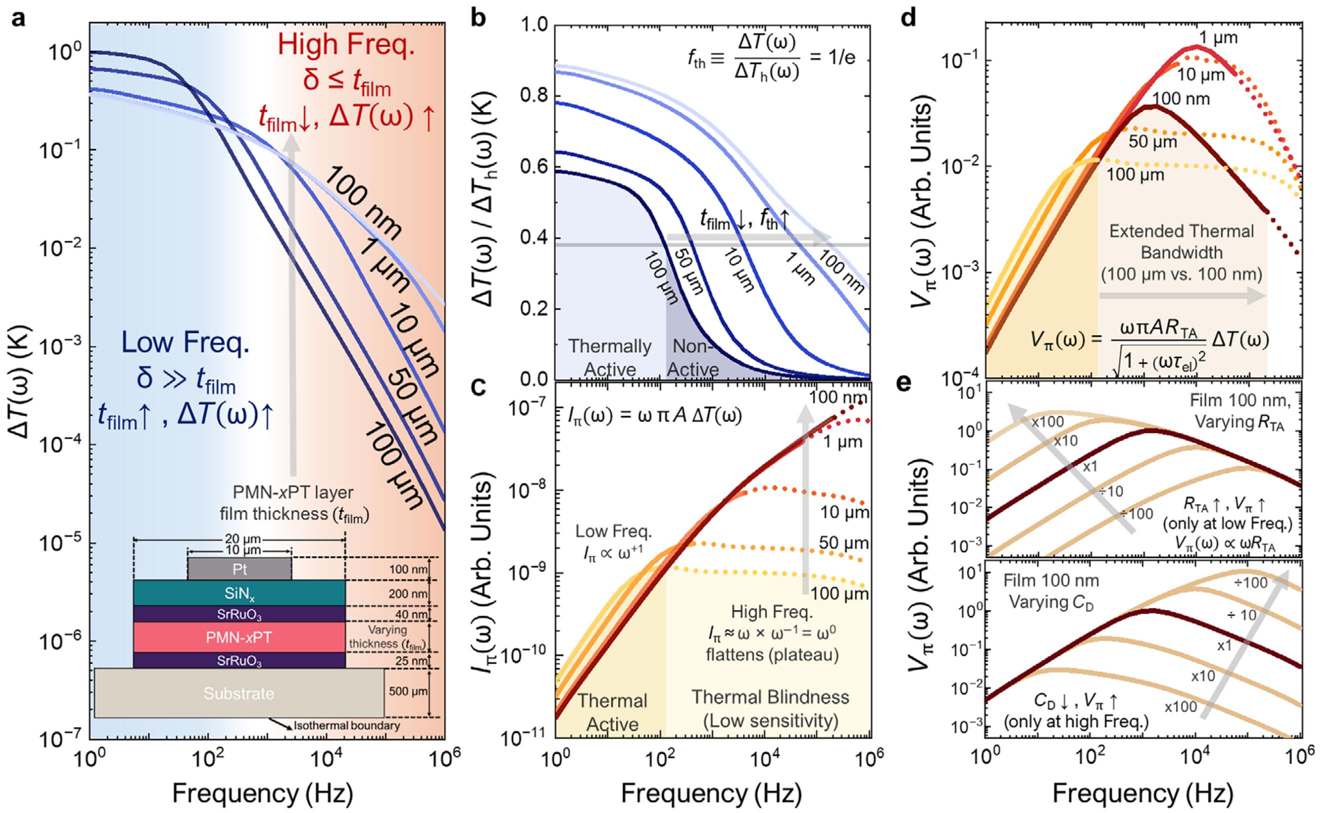

FIGURE 1 | Modeling effects of thickness-dependent thermal sensitivity and electrical responsivity on pyroelectric performance. (a) Average temperature oscillation amplitude, $\Delta T(\omega)$, within the pyroelectric layer as a function of modulation frequency. Inset shows the device geometry used for the COMSOL simulations. The thermal penetration depth is given by $\delta(\omega) = \sqrt{2D/\omega}$, where D is the thermal diffusivity and $\omega = 2\pi f$ represents the angular frequency of the heating power and where π is the number pi. (b) Extracted thermal cut-off frequency (f_{th}) as a function of film thickness, revealing the transition from thermally active to thermally non-active regimes. (c) Numerical modeled frequency-dependent pyroelectric current, $I_\pi(\omega)$. Dotted curves denote the thermally blind regime beyond f_{th}, where temperature oscillations become strongly attenuated. (d) Pyrovoltage electrical responsivity, $V_\pi(\omega)$, obtained through voltage-mode readout using a load impedance $Z(\omega) = \frac{R_L}{1+j\omega\tau_{\text{el}}}$. (e) Modeled $V_\pi(\omega)$ under varying R_{TA} and C_{D} for a 100 nm thin film with its peak electrical responsivity set to 1 V W^{-1}.

voltage-mode sensing, while voltage-mode sensing (benefiting from a much with lower noise floor as compared to current-mode) can sense a minimum temperature change $\Delta T_{\min} \approx 30$ μK. The responsivity peak shifts to ≈1 kHz (>2500 times faster than conventional bulk sensors) with measurable responsivity up to a carrier frequency of 100 kHz, while amplitude-resolved detection of thermal signal envelopes is demonstrated up to a modulation frequency of 15 kHz. These results confirm the ability of the device to simultaneously track high-frequency thermal carriers and faithfully recover dynamically varying thermal envelopes.

2 | Results and Discussion

2.1 | Modeling Thickness-Dependent Thermal Sensitivity and Electrical Responsivity

To understand the evolution of pyroelectric performance, thickness-dependent simulations of thermal sensitivity and electrical responsivity were completed. The thermal sensitivity (Figure 1a), $\Delta T(\omega)$, based on COMSOL modeling, evolves with film thickness (t_{film}) ranging from 100 nm to 100 μm across modulation frequencies from 1 Hz to 1 MHz (Methods, Note S1, and Figure S1 and Table S1). As thermal-modulation frequency increases, heat is progressively localized from the substrate to the thin film, as governed by the thermal penetration depth, $\delta(\omega) = \sqrt{2D/\omega}$ (where D is the thermal diffusivity; Note S2 and Figure S2). With reduced $\delta(\omega)$ at higher frequencies, heat becomes confined within the active layer, and only the near-surface region (i.e., the film) participates in the temperature oscillation. Therefore, for thicker films (e.g., >10 μm), only the portion of the film within $\delta(\omega)$ remains thermally active, while the remaining volume is effectively thermally inactive, leading to a reduced $\Delta T(\omega)$, as averaged over film thickness. In contrast, thinner films (e.g., <1 μm) undergo nearly uniform heating across their entire thickness even at high frequencies (1–100 kHz). Consequently, a 100-nm-thick film shows $\Delta T(\omega)$ more than two (three) orders of magnitude larger than a 100-μm-thick film at 100 kHz (1 MHz). Since the minimum detectable power scales as $P_{\min} \propto 1/\Delta T(\omega)$, nanoscale films intrinsically enable lower detection thresholds owing to their reduced thermal mass.

To quantify the intrinsic thermal-sensing bandwidth of the pyroelectric layer, the thermal cut-off frequency (f_{th}) is introduced, which describes the ability to transduce temperature oscillations from the heater to the pyroelectric layer, and defined here as the frequency at which the $\Delta T(\omega)$ decreases to 1/e of the heater temperature $\Delta T_h(\omega)$ (Figure 1b and Equation (1):

$$f_{th} \equiv \frac{\Delta T(\omega)}{\Delta T_h(\omega)} = 1/e. \tag{1}$$

This 1/e criterion is adapted from the classical definition of the $\delta(\omega)$ [32, 33] and generalized for the multilayer heterostructures used here (Note S3). At frequencies above f_{th}, the film enters a thermal-blindness regime (as illustrated by the non-active regime (gray zone) for the 100-µm film, Figure 1b), where the film experiences severe thermal attenuation and the thermal sensitivity and $\Delta T(\omega)$ decay rapidly. Thinner, nanoscale films thus exhibit a higher f_{th} as compared to thicker films – thus making size reduction to 10–100 nm essential for superior thermally active bandwidths.

Next, the thickness-dependent pyroelectric response was analyzed (Figure 1c). The pyroelectric current generated by a periodic temperature modulation is expressed as:

$$I_\pi(\omega) = \omega\, \pi\, A\, \Delta T(\omega) \tag{2}$$

where A is the effective electrode area. The evolution of I_π with temperature-modulation frequency reveals two distinct regimes separated by f_{th}. For thicker films (e.g., 100 µm), the lower f_{th} causes I_π to plateau at relatively low frequencies (≈130 Hz), indicating early saturation of the same. In contrast, thinner films (e.g., 100 nm) allow I_π to continue to increase up to 100 kHz–1 MHz before leveling off. Therefore, under the same heating power, thinner films can generate higher I_π at higher frequencies as compared to their thicker counterparts, benefiting from smaller thermal mass and broader thermally active bandwidth.

To convert the generated current into measurable voltage, the electrical transduction can be implemented using either current- or voltage-amplifier architectures (Note S4). Here, numerical simulations of voltage-mode operation help identify the electrical limitations imposed by C_D. The simulated pyrovoltage ($V_\pi(\omega)$, Figure 1d) is obtained by converting I_π through a hypothetical voltage amplifier with load resistor R_L, which introduces an $\tau_{el} = R_L\, C_D$. The corresponding $V_\pi(\omega)$ is expressed as:

$$V_\pi(\omega) = |Z(\omega)|\; I_\pi(\omega) = \frac{\omega\, \pi\, A\, R_L}{\sqrt{1 + (\tau_{el}\omega)^2}}\, \Delta T(\omega). \tag{3}$$

The simulations indicate that reducing film thickness (e.g., from 100 µm to 100 nm) extends the thermal bandwidth but simultaneously increases C_D, thereby increasing τ_{el} and limiting the voltage amplitude and electrical bandwidth at high frequencies. This trade-off highlights the central challenge: how does one simultaneously achieve high thermal sensitivity and electrical responsivity for fast-response pyroelectric sensors operating at high modulation frequencies?

Using a 100-nm-thick film as a reference, the influence of the electrical readout parameters was examined. Increasing R_L (top, Figure 1e) enhances $V_\pi(\omega)$ only in the low-frequency regime ($\omega < f_{el}$), where the voltage scales linearly with R_L. At higher frequencies ($\omega > f_{el}$), the response instead decays as $V_\pi(\omega) \propto 1/C_D$, such that R_L no longer contributes to the gain. Reducing C_D (bottom, Figure 1e), however, increases electrical responsivity and extends the high-frequency bandwidth. These competing effects, including increased C_D in thinner films, prolonged τ_{el}, and the intrinsic combination of low π and high ε_r at zero bias in relaxor ferroelectric thin films, motivates the introduction of E_{int} via nanoscale compositional and strain gradients, as discussed in the following sections.

2.2 | Built-In Potential from Compositional and Strain Gradients

To address these competing constraints, strain gradients induced by compositional gradients across the thickness of 100-nm-thick PMN-xPT thin films were explored (Methods). A set of single-composition reference films ($x = 0$, 0.16, 0.32, 0.48, and 0.64) and compositionally graded films [(0.32, 0), (0.48, 0.16), and (0.64, 0.32)] were synthesized on different substrates [i.e., $NdScO_3$ (110), $GdScO_3$ (110), and $DyScO_3$ (110)]. The compositionally graded films are denoted as (x', x'')(substrate), where x' and x'' correspond to the bottom and top compositions in the gradient, respectively. For example, the (0.64, 0.32)($NdScO_3$) heterostructure refers to a compositionally graded film transitioning from $x = 0.64$ at the substrate interface to $x = 0.32$ at the top surface grown on a $NdScO_3$ (110) substrate. Representative compositions were selected based on the bulk PMN-xPT phase diagram [34] (Note S5 and Figure S3a), which evolves from a relaxor region ($x \approx 0$–0.32), across the morphotropic phase boundary (MPB) ($x \approx 0.32$), to a tetragonal, ferroelectric region ($x \gtrsim 0.32$) with increasing $PbTiO_3$ fraction (x).

X-ray diffraction θ–2θ line scans confirm all films are single crystalline films of high quality (Figure S3b,c). Focusing on the 002-diffraction condition for the compositionally graded heterostructures grown on $NdScO_3$ (110) substrates (top three patterns, Figure 2a), relatively broad intensity plateaus for the films extend between the peak positions of single-composition end members (as indicated by dashed lines, Figure 2a). This indicates a reasonably continuous variation in out-of-plane lattice parameters across the film thickness. In contrast, single-composition films (Figure S3b) exhibit well-defined, sharp film peaks shifting to higher 2θ with increasing x, consistent with a transition from compressive (for $x = 0$ films) to tensile (for $x = 0.64$ films) epitaxial strain. Among the three compositionally graded variants studied herein, (0.64, 0.32)-type heterostructures were selected for further study as the higher $PbTiO_3$ content favors out-of-plane polarization, and these heterostructures were subsequently grown on $GdScO_3$ (110) and $DyScO_3$ (110) substrates, which impose progressively larger compressive strains to investigate how substrate-induced strain further impacts the materials. X-ray diffraction θ-2θ scans (bottom three patterns, Figure 2a) reveal systematic shifts of the broad, plateau-like diffraction peaks toward lower angles for heterostructures grown on $NdScO_3$ (110), $GdScO_3$ (110), and $DyScO_3$ (110) – consistent with the progressively increasing compressive strain.

Asymmetric reciprocal-space maps about the 103 (film)- and 332_O (substrate)-diffraction conditions (where O denotes orthorhombic indices) confirm that all compositionally graded films remain coherently strained to the substrates (Figure 2b–f). The diffraction peaks for the compositionally graded films, while aligned in-plane (Q_x) with the substrate, exhibit vertical elongation along

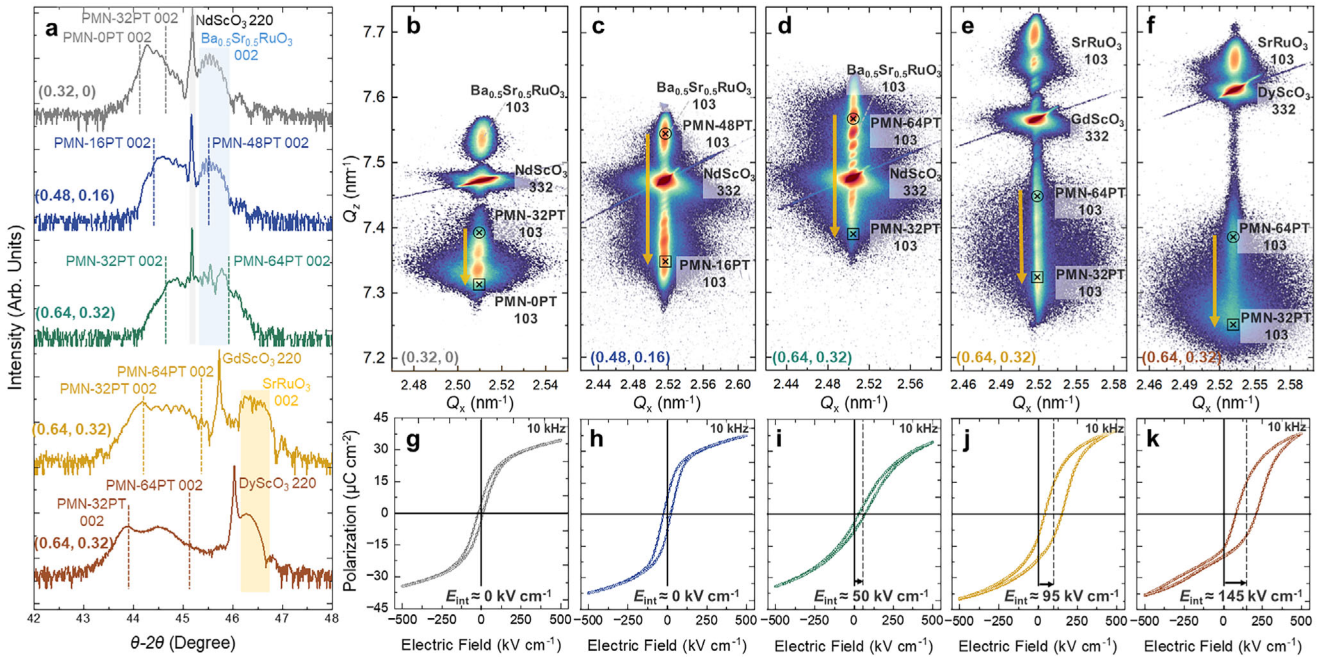

FIGURE 2 | Strain-gradient evolution induced by compositional and epitaxial strain in PMN–xPT thin films. (a) θ–2θ X-ray diffraction line scans for (top to bottom) (0.32, 0)($NdScO_3$), (0.48, 0.16) ($NdScO_3$), (0.64, 0.32)($NdScO_3$), (0.64, 0.32)($GdScO_3$), and (0.64, 0.32)($DyScO_3$) compositionally graded PMN–xPT heterostructures. Reciprocal space maps about the 103-diffraction condition of (b) (0.32, 0)($NdScO_3$), (c) (0.48, 0.16) ($NdScO_3$), (d) (0.64, 0.32)($NdScO_3$), (e) (0.64, 0.32)($GdScO_3$), and (f) (0.64, 0.32)($DyScO_3$) compositionally graded PMN–xPT heterostructures. Polarization–electric field hysteresis loops for (g) (0.32, 0)($NdScO_3$), (h) (0.48, 0.16) ($NdScO_3$), (i) (0.64, 0.32)($NdScO_3$), (j) (0.64, 0.32)($GdScO_3$), and (k) (0.64, 0.32)($DyScO_3$) compositionally graded PMN–xPT heterostructures.

Q_z, indicating variation in the out-of-plane lattice parameter in conjunction with the compositional gradient across the film thickness. Using the diffraction peak positions of the single-composition films (Figure S4) as references (and as annotated on the reciprocal space maps of the compositionally graded films), the average out-of-plane strain gradients across the 100-nm-thick films were extracted as: $\approx 1.1 \times 10^5$, $\approx 1.9 \times 10^5$, and $\approx 2.7 \times 10^5$ m^{-1} for the (0.32, 0)($NdScO_3$), (0.48, 0.16)($NdScO_3$), and (0.64, 0.32)($NdScO_3$) heterostructures, respectively (Figure 2b–d) and $\approx 2.7 \times 10^5$ m^{-1} for the (0.64, 0.32)($GdScO_3$, $DyScO_3$) heterostructures (Figure 2e,f) (details of the analysis are in Note S6 and Tables S2 and S3). For the (0.64, 0.32) heterostructures, although the nominal out-of-plane strain change ($\approx$ 2.7%) is similar across all substrates, the absolute strain state varies systematically from: +1.0% to −0.5% (tensile to compressive) for films on $NdScO_3$ (110) substrates, to −0.07% to −1.5% (nearly matched to compressive) for films on $GdScO_3$ (110) substrates, to −0.5% to −2.0% (fully compressive) for films on $DyScO_3$ (110) substrates. As such, the substrate lattice constant tunes not only the amplitude of the out-of-plane strain gradient but also its sign, transitioning from tensile to compressive-dominated states. The influence of these distinct strain landscapes on polarization behavior is therefore examined.

Polarization–electric field hysteresis loops (Methods, Figure 2g–k) reveal that both the (0.32, 0)($NdScO_3$) (Figure 2g) and (0.48, 0.16)($NdScO_3$) (Figure 2h) heterostructures show nearly symmetric hysteresis loops with negligible shifts along the field axis, indicating minimal E_{int}. The absence of E_{int} in these heterostructures reflects the relatively more relaxor-like nature of the chemistry and the smaller strain gradients. In contrast, the (0.64, 0.32)($NdScO_3$) heterostructures (Figure 2i) exhibit a pronounced shift with $E_{\text{int}} \approx 50$ kV cm^{-1} and an average remanent polarization at zero field (as calculated as the average of the two remanent values) $\bar{P}_r \approx 6$ μC cm^{-2}. In turn, transitioning to the (0.64, 0.32)($GdScO_3$, $DyScO_3$) heterostructures maintains the larger strain gradient and the further compressive strain favors a rotation of the polarization toward the out-of-plane [001] and supports larger $E_{\text{int}} \approx 95$ kV cm^{-1} and $\bar{P}_r \approx 15$ μC cm^{-2} for the (0.64, 0.32)($GdScO_3$) heterostructures (Figure 2j) and $E_{\text{int}} \approx 145$ kV cm^{-1} with $\bar{P}_r \approx 18$ μC cm^{-2} for the (0.64, 0.32)($DyScO_3$) heterostructures (Figure 2k). These results establish a clear correlation between the compositional gradients and the substrate-induced strain in producing E_{int}, offering a route to tailor polarization, dielectric, and pyroelectric responses in relaxor ferroelectric thin films.

2.3 | Evaluation of the Pyroelectric Response in Current Mode

To investigate how nanoscale strain gradients impact the π of the compositionally graded heterostructures with varying E_{int}, electrothermal test devices were fabricated [17, 31] (Methods, Figure 3a). The operating principle is as follows: when the pyroelectric film undergoes a temperature change ΔT, the bound surface charges at the film interfaces are redistributed. During heating ($dT/dt > 0$), the spontaneous polarization decreases by $\Delta P = \pi \cdot \Delta T$, reducing the bound surface charge density. To compensate, free charges flow out through the external circuit, generating a pyroelectric current $I_\pi = \pi \cdot A \cdot (dT/dt)$ directed from the top electrode through the external circuit to the grounded bottom electrode. During cooling ($dT/dt < 0$), the

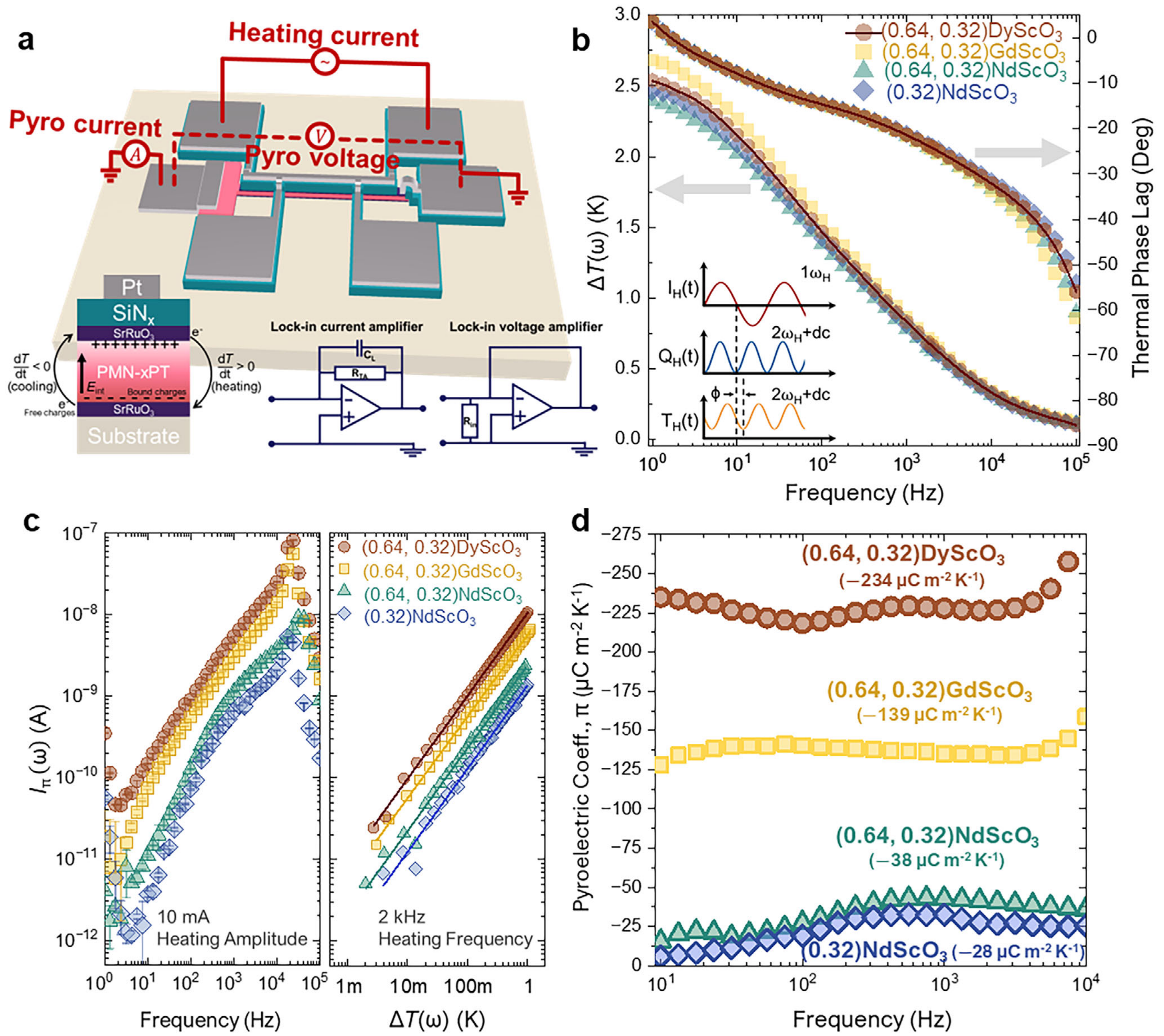

FIGURE 3 | Current-mode pyroelectric measurements. (a) Schematic of the electrothermal test device illustrating the pyroelectric current I_π generation under heating/cooling excitation, and the two readout configurations: current-mode (R_{TA}-based) and voltage-mode (high-impedance mode, $R_L > R_{TA}$) detection. (b) 3ω-based method for determining $\Delta T(\omega)$ and thermal phase lag. $\Delta T(\omega)$ is derived from $\Delta T_h(\omega)$ via COMSOL-simulated correlation factors (Figure S5c). (c) Frequency-dependent pyrocurrent response used to extract the pyroelectric coefficient π (right: 2 kHz heating frequency). Measurements were conducted at zero-bias using a 1 kHz heating current by sweeping the heating-current amplitude from 0.5 to 10 mA in 0.5 mA steps to vary $\Delta T(\omega)$. (d) Extracted π as a function of modulation frequency, highlighting the enhanced (average for this measurement range) π achieved in graded films compared with single-composition counterparts.

spontaneous polarization increases, drawing free charges back into the device and reversing the direction of I_π. In current-mode operation, I_π is directly detected by a lock-in current amplifier in transimpedance configuration. In voltage-mode operation, I_π charges the film capacitance C_D, developing a voltage across the device that is measured by a lock-in voltage amplifier through a high-impedance load resistor R_L. Consistent with the results thus far, the focus here is on the (0.64, 0.32) heterostructures grown on the various substrates as well as single-composition ($x = 0.32$) films grown on $NdScO_3$ (110) as a reference. A lock-in detection technique was employed to measure the pyroelectric response (Methods). Periodic temperature oscillations at $2\omega_H$ were generated by Joule heating, induced through an AC heating current at frequency $1\omega_H$ applied to a platinum heater line (inset, Figure 3b). The $\Delta T(\omega)$ and thermal-phase lag (Figure 3b) were determined using the 3ω method (Note S7 and Figure S5a–d).

The frequency-dependent $I_\pi(\omega)$ (left, Figure 3c) was measured in current-amplifier mode under zero-bias operation using a 1 kHz, 10 mA heating current. All devices exhibit a nearly linear increase of $I_\pi(\omega)$ with modulation frequency on a log–log scale, consistent with modeling results of pyroelectric scaling. To precisely determine π, the heating-current amplitude was swept from 0.5 to 10 mA in 0.5 mA steps at 1 kHz, resulting in varying $\Delta T(\omega)$. The slope, $\pi A 2\omega_c$ on a linear-linear scale, of the plot of $I_\pi(\omega)$ as a function of $\Delta T(\omega)$ (right, Figure 3c) is used to extract the value of π. Among all devices, at a modulation heating frequency of 2 kHz, the (0.64, 0.32)($DyScO_3$) heterostructures exhibit the largest magnitude $\pi \approx -226$ μC m^{-2} K^{-1}; bigger in magnitude than that for the (0.64, 0.32)($GdScO_3$, $NdScO_3$) heterostructures which have values of −134 μC m^{-2} K^{-1} and −43 μC m^{-2} K^{-1}, respectively, and that of the single-composition ($x = 0.32$) films grown on $NdScO_3$ (110) which have a value of −27 μC m^{-2} K^{-1}. A similar trend is observed in the frequency-dependent π spectra (Figure 3d), where the averaged values over the frequency range of 10 Hz to 10 kHz follow the same order: (0.64, 0.32)($DyScO_3$) ($\pi \approx -234$ μC m^{-2} K^{-1}) > (0.64, 0.32)($GdScO_3$) ($\pi \approx -139$ μC m^{-2} K^{-1}) > (0.64, 0.32)($NdScO_3$) ($\pi \approx -38$ μC m^{-2} K^{-1}) > (0.32)($NdScO_3$) ($\pi \approx -28$ μC m^{-2} K^{-1}). These results confirm that a larger E_{int} contributes to enhanced zero-field π in the compositionally graded heterostructures.

2.4 | Evaluation of the Pyroelectric Response in Voltage Mode

The frequency dependence of $V_\pi(\omega)$ (Methods, Figure 4a) was measured in voltage-mode to elucidate how device capacitance and an external voltage amplifier transform $I_\pi(\omega)$ into measurable voltage. The frequency response divides into two regimes: (1) below f_{el}, $V_\pi(\omega)$ increases with frequency as the thermal-diffusion term dominates and (2) above f_{el}, the response rolls off as the τ_{el} limits charge readout. This framework reveals that thermal diffusion controls amplitude scaling, while the electrical RC sets the bandwidth and peak position. To determine τ_{el} and τ_{th} of the pyroelectric thin-film devices, taking the (0.64, 0.32)($DyScO_3$) devices as an example, τ_{el} can be determined from the peak position where $f_{el} \approx$ 1021 Hz and $\tau_{\text{el}} \approx 0.156$ ms. Notably, the peak position directly reflects τ_{el}, and its shift to higher frequencies arises from the suppressed ε_r under strong E_{int}; an effect most pronounced in the (0.64, 0.32)($DyScO_3$) devices. This interpretation is validated by dielectric measurements (Figure 4b), which show that, at zero electric field, the ε_r of the (0.64, 0.32) heterostructures is systematically reduced with increasing compressive strain as compared to that of the ($x = 0.32$)($NdScO_3$) films ($\varepsilon_r = 1058$). Specifically, the ε_r is suppressed by 67% for films grown on $DyScO_3$ (110) ($\varepsilon_r = 353$), by 65% for films grown on $GdScO_3$ (110) ($\varepsilon_r = 368$), and by 11% for films grown on $NdScO_3$ (110) ($\varepsilon_r = 947$). These results further support the role of E_{int}, induced by strain gradients, in reducing dielectric response. In turn, τ_{th} can be estimated from thermal modeling (Figure 1b), indicating that the 100-nm-thick devices exhibit a thermal cut-off frequency on the order of $f_{\text{th}} = 1/(2\pi\tau_{\text{th}}) \approx 100$ kHz, corresponding to $\tau_{\text{th}} \approx 2$ μs, which shorter than τ_{el}, confirming the device bandwidth is electrically limited.

The FoM_V (assuming $c_p = 2.44 \times 10^6$ J m^{-3} K^{-1} for all heterostructures studied herein) [35] of each device was extracted from the linear relationship between the $V_\pi(\omega)$ and $\Delta T(\omega)$ (Figure 4c). At 2 kHz, the (0.64, 0.32)($DyScO_3$) devices exhibited the highest FoM_V ($\approx 2.5 \times 10^{-2}$ m^2 C^{-1}), followed by the (0.64, 0.32)($GdScO_3$) devices ($\approx 1.4 \times 10^{-2}$ m^2 C^{-1}), (0.64, 0.32)($NdScO_3$) devices ($\approx 1.92 \times 10^{-3}$ m^2 C^{-1}), and then the ($x = 0.32$)($NdScO_3$) films ($\approx 8.9 \times 10^{-4}$ m^2 C^{-1}), resulting in 28-, 12.9-, and 1.8-times enhancements, respectively, of the FoM_V as compared to the single-layer films. A similar trend is observed in the frequency-dependent FoM_V spectra (Figure 4d), where the average FoM_V value over the frequency range of 10 Hz–100 kHz follows the same order: (0.64, 0.32)($DyScO_3$) ($\approx 3.0 \times 10^{-2}$ m^2 C^{-1}) > (0.64, 0.32)($GdScO_3$) ($\approx 1.1 \times 10^{-2}$ m^2 C^{-1}) > (0.64, 0.32)($NdScO_3$) ($\approx 1.85 \times 10^{-3}$ m^2 C^{-1}) > ($x = 0.32$)($NdScO_3$) ($\approx 1.48 \times 10^{-3}$ m^2 C^{-1}). The results confirm that the E_{int} simultaneously enhances π and suppresses ε_r, leading to a greater electrical responsivity. Further, the robustness of the effects across the 25°C–150°C temperature range and to repeated thermal cycles (exceeding 10^7 cycles) were measured in both current- and voltage-mode and both found to be stable (Note S8; Figures S7 and S8).

2.5 | Comparison of Dual-Mode Operation and Amplitude-Resolved Thermal Envelope Detection

The current- and voltage-mode readout characteristics of the (0.64, 0.32)($DyScO_3$) devices were evaluated (Methods) (Figure 5a). Current-mode amplifies I_π through a transimpedance amplifier, resulting in ≈ 20-times higher voltage output than voltage-mode operation. The background noise in current-mode operation (≈20 μV) is, however, significantly higher than in voltage-mode operation (≈60 nV), resulting in a minimum temperature change sensitivity $\Delta T_{\text{min}} \approx 0.6$ mK and ≈ 30 μK, respectively, corresponding to an ≈ 20-times improvement in temperature resolution for voltage-mode operation (Figure 5b). This comparison highlights that the dominant electrical constraints differ between the two operation modes. In current-mode operation, electrical bandwidth and noise are governed by the transimpedance amplifier (R_{TA}-C_f network), where R_{TA} introduces gain-dependent Johnson and amplifier noise. In contrast, voltage-mode operation is limited by C_D and R_L, but benefits from a significantly lower intrinsic noise floor (details of the noise analysis are found in Note S9 and Figure S9a–c). In practice, current-mode operation is advantageous for maximizing voltage output, whereas voltage-mode operation is preferable for resolving weak thermal signals under low-noise conditions. Before, one had often to choose one over the other – the approach presented herein makes it possible to have the best of both worlds.

To further demonstrate dynamic, amplitude-resolved thermal sensing at high modulation frequencies (f_{mod}) of the pyroelectric sensor in this work, a practical scenario is considered in which an optical chopper sets a fixed carrier frequency while the thermal signal of interest – such as that from a moving or transiently heated object – constitutes a time-varying amplitude envelope superimposed on the carrier. The signal architecture underlying this scheme is depicted (upper trace, Figure 5c) and represents the time-varying thermal information envelope:

$$A(t) = A_0 \left[1 + m \cdot \cos(2\pi f_{mod} t)\right] \tag{4}$$

where f_{mod} denotes the modulation frequency and m is the modulation depth. The resulting amplitude-modulated thermal carrier signal (lower trace, Figure 5c):

$$S(t) = A(t)\left[1 + m \cdot \cos(2\pi f_{carrier} t)\right] \tag{5}$$

is such that the high-frequency carrier oscillation is gated by the time-varying amplitude envelope. This composite signal encodes the thermal information of interest within the envelope, while the carrier frequency serves as the stable demodulation reference.

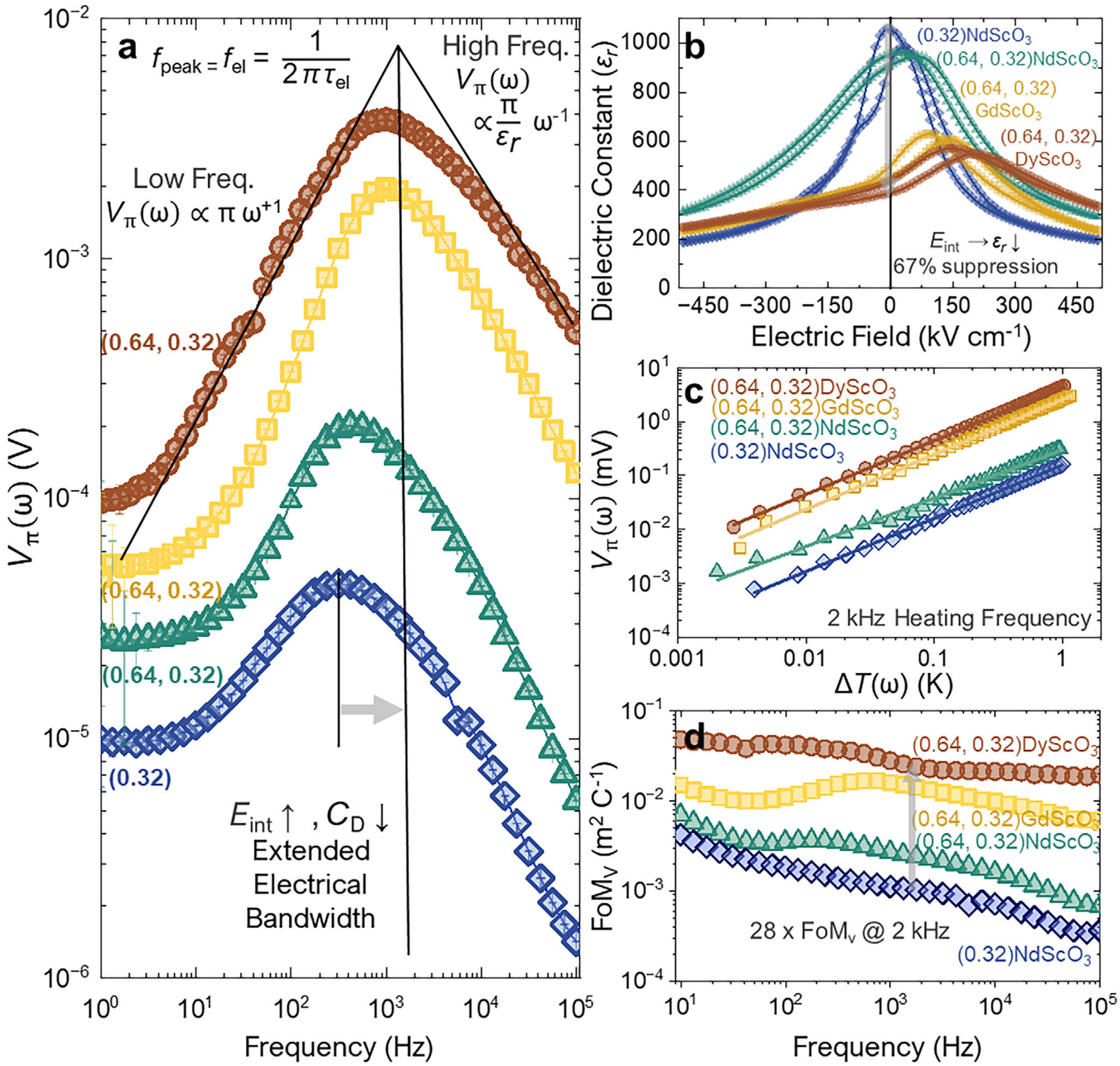

FIGURE 4 | Frequency-dependent, voltage-mode pyroelectric measurements. (a) Frequency-dependent pyrovoltage spectra of compositionally graded and single-composition PMN–xPT thin films measured under lock-in voltage-mode detection. (b) Dielectric permittivity (ε_r) at 10 kHz showing up to 67% suppression in graded films relative to single-composition ($x = 0.32$)($NdScO_3$) (110). (c) Pyroelectric voltage as a function of temperature oscillation at 2 kHz heating frequency. (d) Frequency-dependent spectra of FoM_V.

The experimental implementation (Figure 5d) employs a function generator to simultaneously apply an amplitude-modulated excitation, consisting of carrier frequency $f_{carrier}$ and modulation frequency f_{mod} to the heater-line of the device. The resulting pyroelectric signal is measured using a lock-in amplifier referenced $2f_{carrier}$, which selectively tracks the amplitude variation of the thermal carrier and thereby recovers the time-varying envelope $A(t)$ as the analog output, monitored in real time on an oscilloscope. To experimentally validate this concept, the (0.64, 0.32)($DyScO_3$) heterostructures were measured using a fixed carrier frequency of 50 kHz corresponding to a thermal carrier frequency of 100 kHz, while f_{mod} was varied from 0.1 Hz to 15 kHz (Figure 5e–j, Methods). At low modulation frequencies (0.1–1000 Hz; Figure 5e–g), the recovered envelope closely reproduces the imposed modulation waveform with negligible attenuation, demonstrating faithful amplitude-resolved detection across this entire bandwidth. As f_{mod} increases beyond 1 kHz, progressive amplitude reduction becomes evident: moderate attenuation is first observed at 5 kHz (Figure 5h), whereas stronger decay occurs at 10 and 15 kHz (Figure 5i,j). Despite this attenuation, the magnified insets confirm that the modulation envelope remains clearly distinguishable above the noise floor, indicating that the encoded thermal information can still be recovered. The observed behavior reflects the interplay between two distinct dynamic constraints: the τ_{th} determines whether the modulation envelope can be temporally resolved, whereas the electrical RC

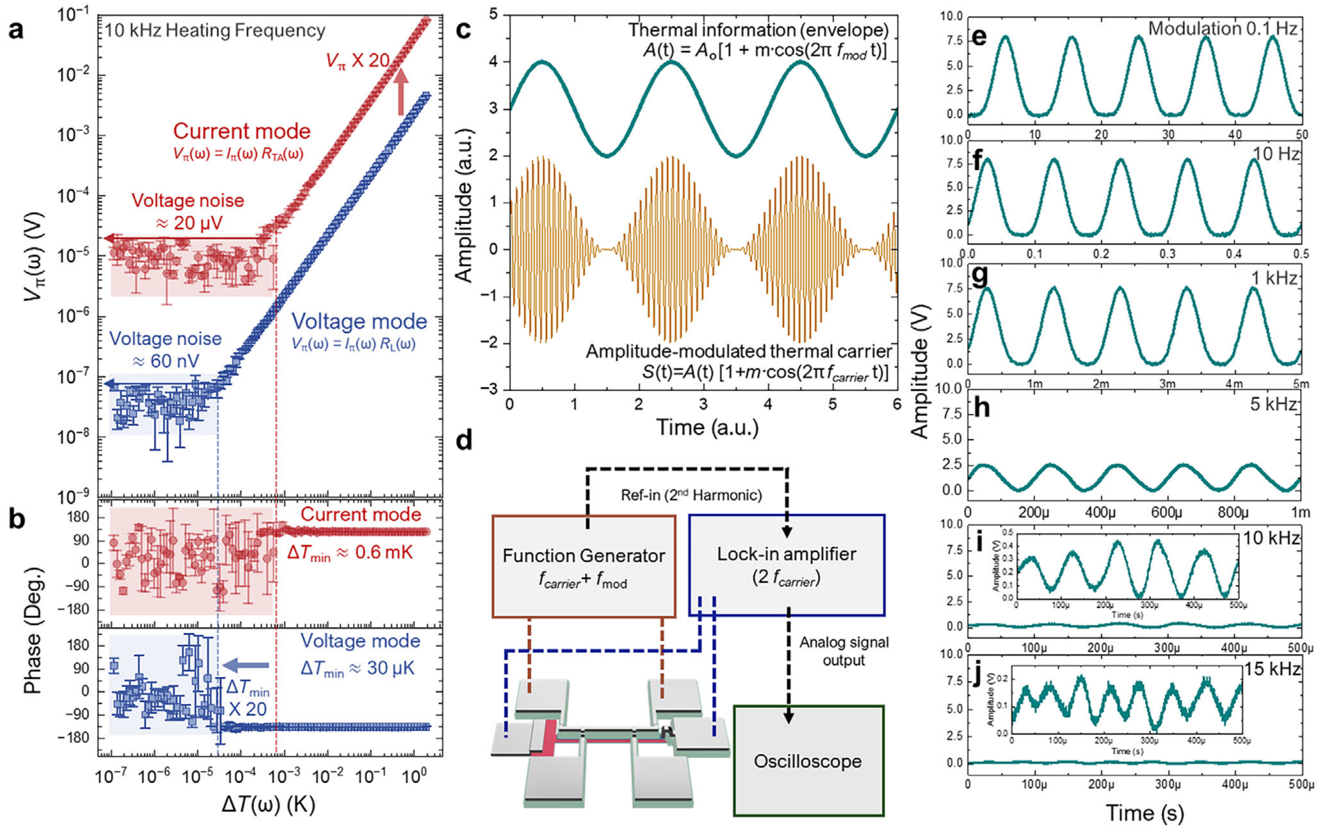

FIGURE 5 | Dual-mode readout characteristics and amplitude-resolved thermal envelope detection. (a) Output voltage amplitude and (b) phase response as a function of temperature oscillation amplitude, $\Delta T(\omega)$, measured using current-mode (R_{TA}= 1 MΩ, $C_f \approx 5$ pF) and voltage-mode (R_L= 10 MΩ, $C_D \approx 100$ pF) readout under heating frequency at 10 kHz. The minimum detectable temperature oscillation, ΔT_{min}, is defined as the temperature modulation amplitude at which the phase fluctuation exceeds ≈ 20°, indicating loss of phase stability and proximity to the background noise. (c) Signal architecture for amplitude-resolved thermal envelope detection, showing the thermal information envelope (upper trace) and the resulting amplitude-modulated thermal carrier signal (lower trace). (d) Schematic of the experimental setup for amplitude-resolved thermal envelope detection. Demodulated envelope waveforms at f_{mod} values of (e) 0.1 Hz, (f) 10 Hz, (g) 1 kHz, (h) 5 kHz, (i) 10 kHz, and (j) 15 kHz, with $f_{carrier}$ fixed at 50 kHz. Insets in (i,j) confirm that the thermal envelope remains resolvable despite RC-induced attenuation at elevated modulation frequencies.

time constant governs the amplitude fidelity of the recovered signal at elevated modulation frequencies. Importantly, even under significant RC-induced attenuation, the periodic thermal envelope remains detectable at modulation frequencies exceeding 10 kHz while the thermal carrier frequency is maintained at 100 kHz. These results establish that nanoscale pyroelectric thin films enable real-time, amplitude-resolved detection of time-varying thermal signals over a broad modulation-frequency bandwidth – a capability inaccessible to conventional bulk sensors operating in the sub-Hz regime [36–41] (Note S10 and Table S4.).

3 | Conclusions

This study examines the fundamental limits of pyroelectric detection from a materials physics and design perspective, particularly the interplay among thermal sensitivity, pyroelectric conversion, and electrical responsivity. While thinner films improve thermal bandwidth by reducing thermal mass, they also increase the capacitance and suppresses electrical responsivity. Nanoscale compositional- and strain-graded PMN–xPT thin films, however, can be engineered to induce E_{int} that enhances the P_r and lowers ε_r at zero field. Combined with geometric thinning, this enables complementary dual-mode operation at zero-bias, yielding a 10-times increase in current-mode responsivity and a 28-times improvement in the FoM_V over uniform-composition films without E_{int}. Voltage-mode operations achieves improved temperature resolution ($\Delta T_{min} \approx 30$ μK), and the response time is reduced by >2500-times relative to commercial bulk sensors, with measurable thermal responsivity extending to a carrier frequency of 100 kHz and amplitude-resolved detection demonstrated up to a modulation frequency of 15 kHz. By linking thermal transport with polarization engineering in nanostructures, this study demonstrates how careful nanoscale engineering bridges the gap between materials design and device functionality for high-frequency, energy-efficient pyroelectric sensors.

4 | Experimental Section/Methods

4.1 | Thermal Modeling

The COMSOL modeling undertaken in this work served two purposes: (i) to investigate how the thickness-dependent thermal mass and thermal penetration depth of the film stack influence the temperature change ($\Delta T(\omega)$) at the PMN-xPT active layer as a function of thermal-modulation frequency, and (ii) to correct for the temperature difference between the heater line and the pyroelectric active layer, ensuring accurate determination of the actual temperature experienced by the layer of pyroelectric film. The thermal sensitivity $\Delta T(\omega)$ of the thickness-dependent pyroelectric layer (Figure 1a) were simulated using COMSOL Multiphysics 6.3 in the 2D frequency-domain perturbation mode (simulation parameters provided in Note S1). A 2D approximation was adopted since the heater length is much greater than the thermal wavelengths corresponding to the modulation frequencies of interest. The top layer, representing the platinum heater, was modeled with uniform Joule heating of 1 W m^{-1}, while domain probes were used to track the complex temperature response of both the heater and the underlying pyroelectric layer. The simulations were then repeated for varying pyroelectric layer thicknesses, while maintaining the identical geometric parameters and boundary conditions, to gain insights into the influence of thickness-dependent in pyroelectric responses. The simulations also provide a thermal penetration depth $\delta(\omega)$ of the pyroelectric device as a function of modulation frequency (Note S2) and frequency-dependent correction factor for 100 nm-thick pyroelectric layer (Figure S5c). Since the experimental 3ω setup measures only the heater temperature, this factor is used to convert the heater temperature oscillation into the corresponding temperature oscillation within the pyroelectric active layer. The resulting $\Delta T(\omega)$ in the active layer is then used for quantifying the pyroelectric coefficient. The input parameters used in the COMSOL model were exclusively thermal properties, specifically the thermal conductivity (k) and specific heat capacity (C) of each constituent layer listed in Table S1. No piezoelectric/dielectric properties (e.g., piezoelectric tensor d_{ij}, dielectric tensor ε_{ij}) or substrate mechanical properties were included in the model.

4.2 | Pulsed-Laser Deposition of Thin-Film Heterostructures

The focus of this work is on heterostructures of two forms. The first was single-composition films of the form 40 nm $Ba_{0.5}Sr_{0.5}RuO_3$/100 nm PMN-xPT (x = 0, 0.16, 0.32, 0.48, and 0.64)/25 nm $Ba_{0.5}Sr_{0.5}RuO_3$, which were deposited on $NdScO_3$ (110) substrates. The second are the compositionally graded films grown on various substrates. For those grown on $NdScO_3$ (110) substrates, the heterostructures were of the form 40 nm $Ba_{0.5}Sr_{0.5}RuO_3$/100 nm compositionally graded PMN-xPT/25 nm $Ba_{0.5}Sr_{0.5}RuO_3$, whereas for those grown on $GdScO_3$ (110) and $DyScO_3$ (110) substrates, the heterostructures were of the form 40 nm $SrRuO_3$/100 nm compositionally graded PMN-xPT/25 nm $SrRuO_3$. All films were synthesized using pulsed-laser deposition with a KrF excimer laser (λ = 248 nm; LPX 300, Coherent, Inc.). Prior to growth, all substrates were ultrasonicated in acetone and then isopropyl alcohol for 10 min each. The substrates were mounted using colloidal silver paste (Ted Pella Inc., PELCO) on a resistive Inconel heater and heated up to 100°C to remove residual solvents and assure a robust thermal connection. Prior to growth, the deposition chamber was pumped down to below 1 × 10^{-5} Torr. For all growths, the target-to-substrate distance was maintained at 58 mm. The growth of the bottom $Ba_{0.5}Sr_{0.5}RuO_3$ layers was performed from a ceramic target of the same chemistry (Praxair Surface Technology) at a heater temperature of 800°C, a laser fluence of 1.8 J cm^{-2}, and a laser repetition frequency of 2 Hz in a dynamic oxygen partial pressure of 20 mTorr. The growth of the bottom $SrRuO_3$ layers was performed from a ceramic target of the same chemistry (Praxair Surface Technology) at a heater temperature of 680°C, a laser fluence of 1.0 J cm^{-2}, and laser repetition frequency of 15 Hz in a dynamic oxygen partial pressure of 100 mTorr. The growth of the PMN-xPT (x = 0, 0.16, 0.32, 0.48, and 0.64) films was performed from ceramic target (Praxair Surface Technology) with 10% lead excess to compensate for lead volatilization, at a deposition temperature of 600°C, a laser fluence of 2.1 J cm^{-2}, and a laser repetition frequency of 2 Hz in a dynamic oxygen partial pressure of 200 mTorr. The compositionally graded PMN-xPT heterostructures, corresponding to the (0.32, 0), (0.48, 0.16), and (0.64, 0.32) heterostructure variants described in the main text, were grown from ceramic targets of $Pb_{1.1}Mg_{1/3}Nb_{2/3}O_3$ and $Pb_{1.1}TiO_3$ using a programmable target rotator (Neocera, LLC) synchronized with the KrF excimer laser. The depositions were performed at 600°C, a laser fluence of 2.1 J cm^{-2}, and a laser repetition frequency of 5 Hz in a dynamic oxygen partial pressure of 200 mTorr, while continuously varying the target from $PbMg_{1/3}Nb_{2/3}O_3$ to $PbTiO_3$ and vice versa to achieve the desired gradient. The repetition frequency was increased to 5 Hz for the graded films to compensate for the slower deposition rate caused by target switching and to maintain a deposition time comparable to that of the single-composition films, thereby minimizing lead loss. Following the PMN-xPT film growth, the top $Ba_{0.5}Sr_{0.5}RuO_3$ and $SrRuO_3$ layers were deposited in situ under the same conditions as the bottom layers, but with a heater temperature of 600°C to prevent further lead loss. After the deposition, all samples were cooled to room temperature in a static oxygen partial pressure of 700 Torr with a cooling rate of 5°C min^{-1}.

4.3 | Structural Characterization

Symmetric θ-2θ linescans and reciprocal space mapping of thin-film heterostructures of single-composition and compositionally graded PMN-xPT heterostructures was performed using the X'Pert 3 MRD diffractometer (Malvern PANalytical), which was equipped with a 1.8 kW copper x-ray source and a hybrid-optic monochromator. This system includes a Bragg-Brentano mirror and a germanium two-bounce monochromator, providing monochromatic K_α radiation with a wavelength of 1.5406 Å. Fixed-incident-optics slits of 1/2° and 1/16° were used for symmetric θ-2θ line scans and reciprocal space mapping studies, respectively, and the same optical configuration (1/2° divergence slit and 1/16°) was utilized for rocking curve measurements. Symmetric θ-2θ scans were collected with a step interval of 0.005° and a scan rate of 0.05° min^{-1} to analyze the out-of-plane crystal structure of both single composition and compositionally graded PMN–xPT films, focusing on the 002-diffraction conditions. Asymmetric RSMs were measured using a frame-based 1D detector mode collecting around the 103 diffraction conditions of the PMN-xPT films and the 332_O-diffraction conditions of $NdScO_3$, $GdScO_3$, and $DyScO_3$ substrates to analyze the out-of-plane lattice parameters and strain states. For the single composition PMN-xPT films grown on $NdScO_3$ (110) substrates, RSMs about the 103-diffraction condition confirmed that films were coherently strained to the substrates. Asymmetric RSMs were measured using a frame-based 1D detector mode with a 0.005° step size and 2500 s per step counting time. Rocking curves about the 002-diffraction conditions were measured for the single composition PMN-xPT films with a step interval of 0.005° and a scan rate of 0.05° min^{-1} to evaluate their crystalline quality.

4.4 | Electrical and Dielectric Measurements

To make devices for these studies, 25-μm-diameter capacitors were defined by standard photolithography after growth. PMMA photoresist was spin-coated at 1000 rpm for 10 s, then 6000 rpm for 30 s, and subsequently baked on a hot plate at 100°C for 300 s. The resist was then exposed under UV light (395 nm) using a shadow mask for 5–10 s and developed for 20 s in Microposit MF-319 developer solution (≈ 2.2% tetramethylammonium hydroxide). For top-electrode patterning, ion milling was performed using an Intlvac Nanoquest system employing an Ar^+ beam under a 500 V beam voltage, 38 mA beam current, and 100 V accelerator voltage. During etching, the sample was maintained at 15°C and rotated at 15 rpm. A 45° incident angle was selected to balance etch uniformity and rate. The etching endpoint was monitored by secondary ion mass spectrometry (SIMS; IMP-EPD, Hiden Analytical) through detection of the Ba^+ and Sr^+ signals to ensure etching precision and control.

Dielectric capacitance was measured with an impedance analyzer (E4990A, Keysight Technologies). Dielectric constant was extracted from the measured capacitance (C) using the formula $C = \frac{\varepsilon_0 \varepsilon_r A}{d}$, where ε_0 is the vacuum permittivity, ε_r is relative permittivity, A represents the capacitor's area, and d is the film thickness. DC-field-dependent measurements used a 50 mV AC drive voltage at 10 kHz, with a DC bias voltage sweeping between ±5 V. Polarization-electric field hysteresis loops were measured by a Radiant Multiferroics II Tester with bipolar triangular waveforms that provide a continuous sweep over an electric-field range of ±500 kV cm^{-1} at a frequency of 10 kHz. In all electrical measurements, the bottom electrode is grounded, such that a positive voltage applied to the top electrode corresponds to an external applied field oriented from top to bottom. The observed shift of the polarization-electric field hysteresis loops (Figure 2g–k) is in the positive field direction, indicating the presence of a built-in electric field, oriented from the bottom to the top electrode.

4.5 | Pyroelectric Device Fabrication

In accordance with previously defined processing methods [17, 31], the development of electrothermal-test platforms used in this study is summarized here. The fabrication of pyroelectric devices involved a sequence of four exposure steps in the photolithography process. For each step, a standard I-line positive photoresist (Mir-701) was spin-coated at 7000 rpm for 60 s to achieve a uniform thickness of approximately 500 nm. The coated samples were then soft baked at 90°C for 90 s, exposed to UV light (370 nm wavelength) using a Heidelberg MLA150 Maskless Aligner with a dose of 250 mJ cm^{-2}, and then post-baked at 100°C for 60 s prior to development. To pattern the tri-layer heterostructures into active strip-like devices, ion milling was performed using an Intlvac Nanoquest system. The ion milling parameters included a 500 V beam voltage, 38 mA beam current, and 100 V accelerator voltage, with the ion beam incident at a 45° angle. In situ secondary ion mass spectrometry (SIMS) was employed during milling to ensure etching precision and control. Next, ≈200-nm-thick SiN_x was deposited as an electrical insulator and thermal conductor layer via plasma-enhanced chemical vapor deposition (PECVD) at 350°C using an Oxford Plasmalab 80plus PECVD system. The gas mixture included NH_3 and 10% SiH_4 in argon, yielding a deposition rate of 7.5 nm min^{-1}. Film thickness was confirmed using a Nanospec/AFT Model 3000 spectroscopic reflectometer. The SiN_x layer was then patterned through an additional photolithography step and etched using reactive-ion etching (RIE) with a gas mixture of 30 sccm O_2 and 90 sccm CF_4 at 100 W RF power. The etching rate was measured at 37 nm min^{-1} on a SEMI RIE system. The final processing step involved defining a resistive heater line atop the device surface. A 5 nm titanium adhesion layer was first deposited by DC sputtering at 20 W under 3.3 mTorr Argon pressure, at a rate of 1.7 nm min^{-1}. This was followed by deposition of a ≈ 100 nm platinum layer, sputtered at 15 W under 7.0 mTorr Argon pressure, with a growth rate of 8.7 nm min^{-1}. Both depositions were performed at room temperature in a high-vacuum chamber with a base pressure of approximately 10^{-8} Torr.

4.6 | Pyroelectric Coefficient Measurements

To quantify the pyroelectric coefficient, temperature oscillations were induced by applying a sinusoidal heating current $I(t) = I_0\, sin(\omega_{\mathrm{H}} t)$, to a metal heater line using a Keithley 6221 current source. The power input based on Joule's law, $P(t) = I(t)^2\, R(t) = \frac{I_0{}^2 R(t)}{2}\, (1 + cos(2\omega_{\mathrm{H}} t))$, leading to temperature oscillations described by $T(t) = T_0 + \Delta T_{\mathrm{h}} cos(2\omega_{\mathrm{H}} t + \psi)$, where ΔT_{h} is the amplitude of temperature oscillations of heater line, and ψ represents the thermal phase lag. It should be noted that each device's platinum heater line may have slight variations in resistance, so applying the same amplitude of heating current can result in different heating power. Therefore, the temperature coefficient of resistance (TCR) for each device was first characterized. Subsequently, the 3ω method was used to extract the temperature rise , enabling fair comparison across different samples (Figure S5a).

The resistance $R(t)$ of the heater line varies with temperature and is given by $R(t) = R_0(1 + \alpha\, \Delta T_{\mathrm{h}} cos(2\omega_{\mathrm{H}} t + \psi) = \mathrm{R}_0 + \Delta\mathrm{R}\, cos(2\omega_{\mathrm{H}}\mathrm{t} + \psi)$, and α is the temperature coefficient of resistance for platinum, defined as $\alpha = \frac{dR}{dT}\, \frac{1}{R_0}$. Using Ohm's law, the voltage across the heater line $V(t) = I(t) \times R(t)$ can be expressed as:

$$I_0 \cos(\omega t) * \left[R_0 + \Delta R\ \cos(2\omega_{\mathrm{H}} t + \psi)\right] = \mathrm{R_0 I_0} \cos(\omega_{\mathrm{H}}\mathrm{t}) + \frac{\Delta \mathrm{R I_0}}{2}\left[\cos(3\omega_{\mathrm{H}}\mathrm{t} + \psi) + \cos(\omega_{\mathrm{H}}\mathrm{t} + \psi)\right].$$

The interaction between the applied heating current (1ω_c) and the resistance oscillation (2ω_{H}) results in a voltage drop along the heater line that appears at the third harmonic (3ω_{H}). The 3ω_{H} term is directly related to the ΔR, which is linked to the temperature oscillation ΔT_{h}, and can be measured by the 3ω method [42, 43]. Given the much larger amplitude of the $1\omega_{\mathrm{H}}$ signal as compared to the $3\omega_{\mathrm{H}}$ signal, a Wheatstone-bridge circuit was employed to nullify the dominant $1\omega_{\mathrm{H}}$ component, allowing for precise detection of the smaller $3\omega_{\mathrm{H}}$ signal. The $3\omega_{\mathrm{H}}$ voltage is given by:

$$V_{3\omega_{\mathrm{H}}} = \frac{\Delta R I_0}{2} = \frac{\alpha R_0 \Delta T I_0}{2}.$$

An SR830 lock-in amplifier measures the $3\omega_{\mathrm{H}}$ voltage fluctuations ($V_{3\omega_{\mathrm{H}}}$) to calculate the average temperature oscillation amplitude of the heater line:

$$\Delta T_{\mathrm{h}} = \frac{2V_{3\omega_{\mathrm{H}}}}{\alpha R_0 I_0} = \frac{2V_{3\omega_{\mathrm{H}}}}{\frac{dR}{dT}\frac{1}{R_0} R_0 I_0} = 2\frac{dT}{dR}\frac{V_{3\omega_{\mathrm{H}}}}{I_0}.$$

The π was determined using two methods: pyrocurrent and pyrovoltage detection. For the pyrocurrent mode, the pyrocurrent $i_{\mathrm{p}}{}^{rms}$ refers to the root-mean-square value of the pyroelectric current was measured at the bottom electrode using an SR830 lock-in amplifier, synchronized to the $2\omega_c$ signal, in relation to the 1ω signal from the Keithley 6221 current source. With known parameters, such as the capacitor area of $A = 5.4 \times 10^{-5}$ cm^{-2}, temperature oscillations of the heater line (ΔT_{h}), and the heating frequency (f, $\omega = 2\pi f$, again, where π is the number pi), the π was determined from the measured pyroelectric current ($i_{\mathrm{p}}{}^{rms}$), expressed as:

$$i_p{}^{rms} = \pi\, A\, \frac{dT}{dt} = \pi\, A\, (2\omega_H \Delta T_h \cos(2\omega_c t + \psi))$$

and hence,

$$\pi = \frac{i_p{}^{amp}}{(A) * \left(2\omega_H * \Delta T_h * \frac{\Delta T}{\Delta T_h}\right)}.$$

$i_{\mathrm{p}}{}^{amp}$ refers to the peak amplitude of the pyroelectric current. A correction factor, defined as $\frac{\Delta T}{\Delta T_{\mathrm{h}}}$ is introduced to accurately quantify temperature oscillations experienced by the pyroelectric films, defined as the ratio of the average temperature oscillation in the pyroelectric layer to that in the heater line.

The average temperature rise within each region was computed using a 2D finite-element simulation in COMSOL Multiphysics. Specifically, the spatially averaged temperature oscillation in the pyroelectric layer is given by:

$$\Delta T = \frac{1}{W_{PE} * t_{PE}} \int_0^{t_{PE}} \int_0^{W_{PE}} \Delta T\ (x, z)\ dx\, dz,$$

and the corresponding average temperature oscillation in the heater line is:

$$\Delta T_h = \frac{1}{W_H * t_H} \int_0^{t_H} \int_0^{W_H} \Delta T\ (x, z)\, dx\, dz.$$

where W_{PE} *and* t_{PE} are the width and thickness of the pyroelectric layer, and W_H *and* t_H are the width and thickness of the heater line, respectively.

4.7 | Pyroelectric Frequency Modulation Measurements

The frequency-dependent pyroelectric response was measured in both pyrocurrent- (Figure 3d) and pyrovoltage- (Figure 4a) detection modes. For the pyrocurrent-detection mode, the detector interacts with a trans-impedance amplifier ($R_{\mathrm{TA}} = 1$ Mω) with very small input impedance (1 kω with virtual ground). And, for the pyrovoltage-detection mode, the detector interacts with an amplifier of high input impedance ($R_{\mathrm{in}} = 10$ Mω, $C_{\mathrm{L}} =$ 25 pF). In this work, Stanford Research Systems SR830 (maximum frequency up to 102.4 kHz) lock-in amplifier was used. Here, it should be noted that for the pyrocurrent measurement, the RC delay (due to the SR830 model's operational amplifier design featuring a 1 Mω feedback resistor) results in an electrical cutoff frequency of approximately 14–20 kHz (Figure 3d).

In voltage-mode detection, the lock-in amplifier is often assumed to measure the open-circuit pyroelectric voltage, $V_{\mathrm{oc}} = \pi \Delta T / C_{\mathrm{D}}$. The input terminal of the instrument, however, is not a perfect open circuit ($R_{\mathrm{L}} = \infty$, $C_{\mathrm{in}} = 0$) but rather a high-impedance network, typically defined by a parallel combination of input resistance R_{L} (10–100 Mω) and parasitic capacitance C_{L} (10–100 pF). Under periodic heating, the pyroelectric element behaves as a current source $I_\pi = \pi A \frac{dT}{dt}$ parallel with its intrinsic capacitance $C_{\mathrm{D}} = \frac{\varepsilon_o \varepsilon_r A}{d}$. The detected voltage (High-Z/quasi-open-circuit) the measured spectrum is $V_\pi(\omega) = I_\pi(\omega)\,|Z_{\mathrm{L}}(\omega)|$, where $Z_{\mathrm{in}}(\omega) = R_{\mathrm{L}}\ ||\ \frac{1}{j\omega C_D}$ and $V_\pi(\omega) = \omega\pi A\ \Delta T(\omega)\ \frac{R_{\mathrm{L}}}{\sqrt{1+(\tau_{el}\omega)^2}}$. At low frequency ($\omega < \tau_{\mathrm{el}}$), $V_\pi(\omega) \propto \omega\pi$; while at high frequency ($\omega > \tau_{\mathrm{el}}$), $V_\pi(\omega) \propto \frac{\pi}{\varepsilon_r}$. Therefore, using a lock-in amplifier with input impedance to determine the $\mathrm{FOM}_{\mathrm{V}}^{elec} = \frac{\pi}{\varepsilon_r}$ is valid when modulation frequency $> f_{\mathrm{el}}$. Under the open-circuit approximation for a parallel-plate capacitor structure, the pyroelectric voltage can also be expressed as:

$$\Delta V_\pi(\omega) = \frac{\Delta Q}{C} = \frac{\pi\ (A)\ \Delta T(\omega)}{\frac{\varepsilon_o \varepsilon_r A}{d}} = \frac{\pi\, d}{\varepsilon_o \varepsilon_r}\ \Delta T(\omega).$$

where ΔQ is the change in electric charge, C is the capacitance, d is the thickness of the material, A is the area of the capacitor, ε_o is the permittivity of free space, ε_r is the relative permittivity of the material.

4.8 | Dynamic Amplitude-Modulation Detection

An amplitude-modulated sinsoidal heating source was generated using a waveform function generator (Keysight 33500B) at a carrier frequency $f_{\mathrm{carrier}} = 50$ kHz with an applied voltage of 2 V_{rms}. The lock-in amplifier was referenced to the second harmonic of the ($f_{\mathrm{carrier}} = 100$ kHz) to demodulate the pyroelectric response, since resistive Joule heating scales as power $\propto$ voltage [2]. A time-varying modulation envelope at frequency f_{mod}, swept from 0.1 Hz to 15 kHz with modulation depth ($m = 1$), was superimposed on the carrier to generate a dynamically varying thermal signal. For each fixed f_{mod}, the demodulated lock-in output tracking the thermal envelope was recorded as a function of time to characterize the time-domain pyroelectric response. Due to the high sampling rate required to resolve the time-varying envelope, the analog output of the lock-in amplifier (Ch1, Y-channel, Stanford Research Systems SR830) was connected to an oscilloscope (Keysight DSO-X 4024A) for data acquisition. The voltage output was obtained as $V_{out} = \frac{V_{signal}}{Sensitivity} \times 10\ V$, and the lock-in time constant was set at 30 μs at 24 dB/oct roll-off to ensure sufficient sampling and accurate signal detection.

Author Contributions

C.-C.L., T.J.P., and L.W.M. conceived the project. T.J.P., T.Y.K., and J. K. synthesized the films. T.J.P., T.Y.K performed their crystal structure characterization using x-ray diffraction. C.-C.L., T.J.P., and D. K. fabricated various device structures. C.-C.L. performed the pyroelectric measurements. A.B. performed thermal simulations based on COMSOL. C.-C.L., T.J.P. and T.Y.K. performed ferroelectric and dielectric measurements. C.-C.L., T.J.P., A.B., D.L., Z. T., S. P., J. K., and L.W.M. graphed and analyzed the data. C.-C.L., T.J.P., and L.W.M., co-wrote the first draft of the manuscript. A.B. and C.D. gave important advice on manuscript revisions. All authors read and reviewed the data and manuscript.

Acknowledgements

This research was sponsored by the Army Research Laboratory and was accomplished under Cooperative Agreement Number W911NF-24-2-0100. The views and conclusions contained in this document are those of the authors and should not be interpreted as representing the official policies, either expressed or implied, of the Army Research Laboratory or the U.S. Government. The U.S. Government is authorized to reproduce and distribute reprints for Government purposes notwithstanding any copyright notation herein. C.-C.L. acknowledges the support of the Army Research Office under grant W911NF-21-1-0118 and the Taiwan Major Fields Scholarship from the Ministry of Education in Taiwan. T.J.P acknowledges the support of the National Research Foundation of Korea (NRF) grant funded by the Korea government (MSIT) (No. RS-2025-25441800). T.Y.K. and D.L. acknowledges the support of the Army Research Office under grant W911NF-21-1-0126. D.K. acknowledges the support of the National Science Foundation under grant DMR-2329111. Z.T. acknowledges the support of the Office of Naval Research under Grant ONR N000142612045. J.K. acknowledges the support of the Army Research Office under the ETHOS MURI via cooperative agreement W911NF-21-2-0162. J.K. and L.W.M. acknowledge that this material is based upon work supported by the Air Force Office of Scientific Research under award number FA9550-24-1-0266. Any opinions, findings, and conclusions or recommendations expressed in this material are those of the author(s) and do not necessarily reflect the views of the United States Air Force. S.P. acknowledges the support of the U.S. Department of Energy, Office of Science, Office of Basic Energy Sciences, under Award Number DE-SC-0012375 for the development of novel ferroic films.

Conflicts of Interest

The authors declare no conflicts of interest.

Data Availability Statement

The data that support the findings of this study are available from the corresponding author upon reasonable request.

References

1. R. W. Whatmore and S. J. Ward, "Pyroelectric Infrared Detectors and Materials—A Critical Perspective," *Journal of Applied Physics* 133 (2023): 080902, https://doi.org/10.1063/5.0141044.

2. V. Gupta, Z. Mallick, A. Choudhury, and D. Mandal, "On-Demand MXene-Coupled Pyroelectricity for Advanced Breathing Sensors and IR Data Receivers," *Langmuir* 40 (2024): 8897–8910, https://doi.org/10.1021/acs.langmuir.4c00074.

3. D. K. T. Ng, L. Xu, Y. H. Fu, et al., "CMOS AlN and ScAlN Pyroelectric Detectors With Optical Enhancement for Detection of CO_2 and CH_4 Gases," *Advanced Electronic Materials* 9 (2023): 2300622, https://doi.org/10.1002/aelm.202300256.

4. J. Si, X. Xiao, Y. Zhang, et al., "Pyroelectric Properties and Applications of Lithium Tantalate Crystals," *Crystals* 14 (2024): 579, https://doi.org/10.3390/cryst14070579.

5. C. Arose, R. E. Peale, A. C. Terracciano, C. J. Fredricksen, and S. S. Vasu, "Spectrally Selective Lithium Tantalate Pyroelectric Terahertz Detector," *IEEE Sensors Journal* 24 (2024): 27429–27435, https://doi.org/10.1109/JSEN.2024.3425721.

6. A. Sharma, V. Gupta, J.-G. Son, et al., "Linearity of Fast and Highly Sensitive $LiTaO_3$ Pyroelectric Detectors in the Terahertz Range," *IEEE Transactions on Terahertz Science and Technology* 14 (2024): 823–829, https://doi.org/10.1109/TTHZ.2024.3445603.

7. C.-C. Chan, M.-C. Kao, and Y.-C. Chen, "Effects of Membrane Thickness on the Pyroelectric Properties of $LiTaO_3$ Thin Film IR Detectors," *Japanese Journal of Applied Physics* 44 (2005): 951, https://doi.org/10.1143/JJAP.44.951.

8. K. Zhang, W. Luo, X. Zeng, et al., "Integration and Characterization of $LiTaO_3$ Single Crystal Film Pyroelectric Sensor Using Mid-Infrared Metamaterial Perfect Absorber," *IEEE Sensors Journal* 22 (2022): 10381–10387, https://doi.org/10.1109/JSEN.2022.3166527.

9. X. Zeng, W. Luo, K. Zhang, et al., "Wafer-Scale Fabrication of Silicon-Based $LiTaO_3$ Pyroelectric Infrared Detectors by Bonding and Thinning Technology," *IEEE Sensors Journal* 22 (2022): 17721–17726, https://doi.org/10.1109/JSEN.2022.3195772.

10. S. L. Bravina, N. V. Morozovsky, A. N. Morozovska, S. Gille, J.-P. Salvestrini, and M. D. Fontana, "Investigations of $LiNbO_3$ and $LiTaO_3$ Single Crystals for Pyroelectric Applications in the Wide Temperature Range," *Ferroelectrics* 353 (2007): 202–211.

11. H. P. Beerman, "Investigation of Pyroelectric Material Characteristics for Improved Infrared Detector Performance," *Infrared Physics* 15 (1975): 225–231, https://doi.org/10.1016/0020-0891(75)90036-6.

12. L. Li, X. Zhao, X. Li, et al., "Scale Effects of Low-Dimensional Relaxor Ferroelectric Single Crystals and Their Application in Novel Pyroelectric Infrared Detectors," *Advanced Materials* 26 (2014): 2580–2585, https://doi.org/10.1002/adma.201304546.

13. C. Guo, L. Xu, D. Wang, et al., "Giant Pyroelectricity via Doping and Interface Engineering," *Joule* 8 (2024): 3426–3435, https://doi.org/10.1016/j.joule.2024.09.009.

14. Y. Lu, L. Liu, R. Gao, et al., "Ultrafast near-infrared Pyroelectric Detector Based on Inhomogeneous Plasmonic Metasurface," *Light: Science & Applications* 13 (2024): 241, https://doi.org/10.1038/s41377-024-01572-5.

15. J. W. Stewart, J. H. Vella, W. Li, S. Fan, and M. H. Mikkelsen, "Ultrafast Pyroelectric Photodetection With On-Chip Spectral Filters," *Nature Materials* 19 (2020): 158–162, https://doi.org/10.1038/s41563-019-0538-6.

16. V. Fuflyigin, E. Salley, A. Osinsky, and P. Norris, "Pyroelectric Properties of AlN," *Applied Physics Letters* 77 (2000): 3075–3077, https://doi.org/10.1063/1.1324726.

17. S. Pandya, J. Wilbur, J. Kim, et al., "Pyroelectric Energy Conversion With Large Energy and Power Density in Relaxor Ferroelectric Thin Films," *Nature Materials* 17 (2018): 432–438, https://doi.org/10.1038/s41563-018-0059-8.

18. A. Savage, "Pyroelectricity and Spontaneous Polarization in $LiNbO_3$," *Journal of Applied Physics* 37 (1966): 3071–3072, https://doi.org/10.1063/1.1703164.

19. S. T. Popescu, A. Petris, and V. I. Vlad, "Interferometric Measurement of the Pyroelectric Coefficient in Lithium Niobate," *Journal of Applied Physics* 113 (2013): 043101, https://doi.org/10.1063/1.4788696.

20. J. Karthik, J. C. Agar, A. R. Damodaran, and L. W. Martin, "Effect of 90° Domain Walls and Thermal Expansion Mismatch on the Pyroelectric Properties of Epitaxial $PbZr_{0.2}Ti_{0.8}O_3$ Thin Films," *Physical Review Letters* 109 (2012): 257602, https://doi.org/10.1103/PhysRevLett.109.257602.

21. Y.-W. Chen, T.-Y. Yu, C.-W. Huang, et al., "An Electrode Design Strategy to Minimize Ferroelectric Imprint Effect," *Advanced Science* 12 (2025): 70011, https://doi.org/10.1002/advs.70011.

22. A. R. Damodaran, E. Breckenfeld, Z. Chen, S. Lee, and L. W. Martin, "Enhancement of Ferroelectric Curie Temperature in $BaTiO_3$ Films via Strain-Induced Defect Dipole Alignment," *Advanced Materials* 26 (2014): 6341–6347, https://doi.org/10.1002/adma.201400254.

23. S.-C. Lin, C.-T. Kuo, R. B. Comes, et al., "Interface Properties and Built-In Potential Profile of a $LaCrO_3/SrTiO_3$ Superlattice Determined by Standing-Wave Excited Photoemission Spectroscopy," *Physical Review B* 98 (2018): 165124, https://doi.org/10.1103/PhysRevB.98.165124.

24. H. Li, C. R. Bowen, H. Dan, and Y. Yang, "Pyroelectricity Induced by Schottky Interface Above the Curie Temperature of Bulk Materials," *Joule* 8 (2024): 401–415, https://doi.org/10.1016/j.joule.2023.12.006.

25. A. R. Damodaran, S. Pandya, Y. Qi, et al., "Large Polarization Gradients and Temperature-Stable Responses in Compositionally-Graded Ferroelectrics," *Nature Communications* 8 (2017): 14961, https://doi.org/10.1038/ncomms14961.

26. J. C. Agar, A. R. Damodaran, M. B. Okatan, et al., "Highly Mobile Ferroelastic Domain Walls in Compositionally Graded Ferroelectric Thin Films," *Nature Materials* 15 (2016): 549–556, https://doi.org/10.1038/nmat4567.

27. R. V. K. Mangalam, J. C. Agar, A. R. Damodaran, J. Karthik, and L. W. Martin, "Improved Pyroelectric Figures of Merit in Compositionally Graded $PbZr_{1-x}Ti_xO_3$ Thin Films," *ACS Applied Materials & Interfaces* 5 (2013): 13235–13241, https://doi.org/10.1021/am404228c.

28. N. W. Schubring, J. V. Mantese, A. L. Micheli, A. B. Catalan, and R. J. Lopez, "Charge Pumping and Pseudopyroelectric Effect in Active Ferroelectric Relaxor-type Films," *Physical Reviews Letters* 68 (1992): 1778, https://doi.org/10.1103/PhysRevLett.68.1778.

29. S.-H. Baek, M. S. Rzchowski, and V. A. Aksyuk, "Giant Piezoelectricity in PMN-PT Thin Films: Beyond PZT," *MRS Bulletin* 37 (2012): 1022–1029, https://doi.org/10.1557/mrs.2012.266.

30. U. Trstenjak, N. Daneu, J. Belhadi, et al., "Non-stoichiometry and Its Implications for the Properties of PMN–PT Thin Films," *Journal of Materials Chemistry C* 11 (2023): 1144–1154, https://doi.org/10.1039/D2TC04070K.

31. C.-C. Lin, Y. Hu, J. Kim, et al., "Domain-Wall Enhanced Pyroelectricity," *Physical Review X* 15 (2025): 011063, https://doi.org/10.1103/PhysRevX.15.011063.

32. H. S. Carslaw and J. C. Jaeger, Conduction of Heat in Solids, 2nd ed., Clarendon, Oxford, 1959.

33. D. G. Cahill, "Thermal Conductivity Measurement from 30 to 750 K: the 3ω Method," *Review of Scientific Instruments* 61 (1990): 802–808, https://doi.org/10.1063/1.1141498.

34. F. Li, S. Zhang, D. Damjanovic, L. Chen, and T. R. Shrout, "Local Structural Heterogeneity and Electromechanical Responses of Ferroelectrics: Learning From Relaxor Ferroelectrics," *Advanced Functional Materials* 28 (2018): 1801504, https://doi.org/10.1002/adfm.201801504.

35. H. Uršič, M. Vrabelj, L. Fulanovič, A. Bradeško, S. Drnovšek, and B. Malič, "Specific Heat Capacity and Thermal Conductivity of the Electrocaloric (1-x)$Pb(Mg_{1/3}Nb_{2/3})O_3$–$PbTiO_3$ Ceramics Between Room Temperature and 300°C," *Journal of Microelectronics, Electronic Components and Materials* 45 (2015): 260–265.

36. InfraTec Infrared Sensors, LME-316 Single Channel Pyroelectric Detector Datasheet, Dresden, Germany, https://www.infratec-infrared.com/sensor-division/single-channel-detectors/.

37. N. Neumann, A. Kaiser, and D. Mutschall, "Advantages and Limitation of Mn Doped PIN–PMN–PT Single Crystals in Pyroelectric Detectors," *APL Materials* 9 (2021): 021106, https://doi.org/10.1063/5.0034665.

38. M. Fattori, S. Cardarelli, J. Fijn, et al., "A Printed Proximity-Sensing Surface Based on Organic Pyroelectric Sensors and Organic Thin-Film Transistor Electronics," *Nature Electronics* 5 (2022): 289–299, https://doi.org/10.1038/s41928-022-00762-6.

39. A. Odon and A. Szlachta, "Voltage Response of a Pyroelectric Detector to a Single Rectangular Optical Radiation Pulse," *Sensors* 22 (2022): 6265, https://doi.org/10.3390/s22166265.

40. Z. Wu, M. Zhang, X. Jiang, et al., "Lead-Free Pyroelectric Infrared Detector Based on $(Bi_{1/2}Na_{1/2})TiO_3$-$BaTiO_3$ Ferroelectric Ceramics," *Journal of the American Ceramic Society* 106 (2023): 6755–6761, https://doi.org/10.1111/jace.19299.

41. C. Cai, H. Zhang, B. Li, et al., "Proton Irradiation Effects on the Pyroelectric Properties of P-Type Bismuth Antimonide/Poly(vinylidene fluoride–trifluoroethylene) Composite Films," *Advanced Electronic Materials* 9 (2023): 2201084, https://doi.org/10.1002/aelm.202201084.

42. T. Yamane, N. Nagai, S. Katayama, and M. Todoki, "Measurement of Thermal Conductivity of Silicon Dioxide Thin Films Using a 3ω Method," *Journal of Applied Physics* 91 (2002): 9772–9776, https://doi.org/10.1063/1.1481958.

43. C. Dames, "Measuring the Thermal Conductivity of Thin Films: 3 Omega and Related Electrothermal Methods," *Annual Review of Heat Transfer* 16 (2013): 7–49, https://doi.org/10.1615/AnnualRevHeatTransfer.v16.20.

Supporting Information

Additional supporting information can be found online in the Supporting Information section.

Supporting File: adma73909-sup-0001-SuppMat.pdf.